

Flexible Units Induced Three-Dimensional Covalent Organic Frameworks with a Heteromotif Molecular Junction for Photocatalytic H₂O₂ Production

Jia-Peng Liao,[§] Mi Zhang,[§] Pei Huang, Long-Zhang Dong, Tian-Tian Ma, Guo-Zhang Huang, Yu-Fei Liu, Meng Lu,^{*} Shun-Li Li, and Ya-Qian Lan^{*}



Cite This: *ACS Catal.* 2024, 14, 3778–3787



Read Online

ACCESS |

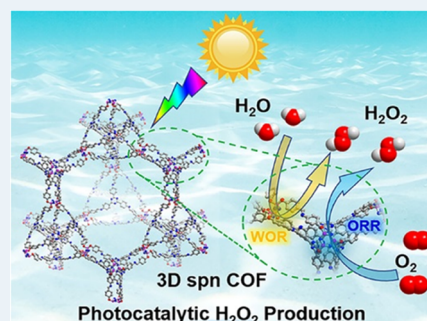
Metrics & More

Article Recommendations

Supporting Information

ABSTRACT: In recent years, significant progress has been achieved in the field of three-dimensional covalent organic frameworks (3D COFs). However, there is still a great challenge to use flexible building units to synthesize high-connectivity 3D COFs. In this work, we showed that [6 + 3] 3D COFs could be constructed by inducing highly flexible planar building blocks from C₃ antitriangular prisms 3D building blocks. Herein, two 3D COFs with spn topology based on flexible cyclotriphosphazene units were constructed and denoted as TAA/TAB-CTP-COF, and their redox ability and photophysical features can be finely regulated by the coupled functional group, such as benzene and triazine groups. As a result, the redox heteromotif molecular junction TAA-CTP-COF with fully exposed active sites achieved high photocatalytic production of hydrogen peroxide (H₂O₂) with a yield of 1041 $\mu\text{M h}^{-1}$ without any additional photosensitizers, organic scavengers, or cocatalysts. Furthermore, in the presence of an electron donor, the production rate of H₂O₂ could reach up to 2221 $\mu\text{M h}^{-1}$, exhibiting one of the best performances for photocatalytic H₂O₂ production in the field of crystalline materials. This work showcases the potential of using flexible building blocks in building 3D COFs and highlights the versatility and efficacy of metal-free COFs in solar energy conversion.

KEYWORDS: covalent organic frameworks, three-dimensional structures, redox heteromotif molecular junction, hydrogen peroxide, photocatalysis



INTRODUCTION

Covalent organic frameworks (COFs), as a kind of crystalline organic porous materials connected by covalent bonds, have attracted wide attention and application due to their good chemical stability and designability, such as gas storage and separation, catalysis, energy storage, and conversion.^{1–3} Since the development of COFs, many two-dimensional (2D) COFs have been reported. Compared with 2D COFs, three-dimensional (3D) COFs with higher specific surface area, interconnected pores,^{4–7} well-exposed functional parts, and highly adjustable structures have undergone great interests.^{8,9} However, due to the limitation of 3D organic building units and crystallization difficulties, 3D COFs are often relatively less developed.^{10,11} Up to now, the design and synthesis of specific 3D COFs depend largely on building units with appropriate geometric shapes. Especially, as an important branch of 3D COFs, currently reported six-connected COFs, such as *ceq* [6 + 3],¹² *stp* [6 + 4],¹³ and *acs* [6 + 6]¹⁴ topology COFs, are still limited to restricted rigid building elements, and expanding the construction of monomers of 3D COFs remains a great challenge.

Apart from rigid building blocks, flexible building blocks also constitute one broad category that can be used for constructing

3D COFs.¹⁵ In general, rigid building blocks are certain and stable in spatial conformations and have lower rotational degrees of freedom, while flexible building elements have different conformations and high degrees of freedom.¹⁶ Through the induction of second building blocks, flexible building blocks can be used for forming 2D or 3D COFs. For example, when a flexible building block is connected to a simple rigid C₂ building block, the synthesized COF is more prone to stacking in the conjugate direction, which leads to the formation of 2D COFs.¹⁷ When flexible building elements are twisted to form a 3D spatial layout, the construction of 3D COFs becomes possible. However, the design of such COFs is still in its infancy;¹⁸ one of the main reasons is that the high degree of freedom of the building block makes it difficult to obtain an ordered arrangement and crystalline properties. Therefore, it is significant to explore new methodologies and

Received: December 14, 2023

Revised: February 3, 2024

Accepted: February 8, 2024

design reasonable building blocks to achieve the synthesis of specific flexible-unit-based 3D COFs. In addition, with regard to the application studies, many previously reported 3D COFs demonstrate low catalytic activity as they are composed of only C, N, O, and H elements, especially for photocatalytic reactions. It is well-known that doping with heteroatoms such as N and P can effectively regulate the optical properties of photocatalysts and also be used as active sites, thereby effectively regulating the photocatalytic performance.^{19–22} Therefore, designing flexible building blocks containing N, P, and O active sites to construct 3D COFs will be a good solution when they are used for photocatalysis.

In the field of photocatalysis, extensive attention has been focused on the artificial photosynthesis of H₂O₂.^{23–31} However, there are many several problems in this field: (i) many photocatalysts have underdeveloped pores or unclear crystal structures, resulting in less exposure of catalytic sites and difficult-to-study catalytic mechanisms; (ii) sacrificial agents need to be added as the band gap of photocatalysts is unable to meet the conditions for simultaneous oxygen reduction reaction (ORR) and water oxidation reaction (WOR); (iii) the contained metal atom in photocatalytic materials will decompose, and the generated H₂O₂ thus causes low yields.³² Hence, rationally designed catalysts that meet all of the above requirements are of crucial importance. Fortunately, 3D COFs with reticular frameworks ensure the precise structure and uniform distribution of active sites,³³ and the well-designed redox junction can be used for simultaneous photocatalytic WOR and ORR to H₂O₂ to avoid the use of sacrificial agents.³⁴ In addition, the further decomposition of H₂O₂ can be prevented when using metal-free COFs, thus reflecting the actual performance over this type of photocatalyst.

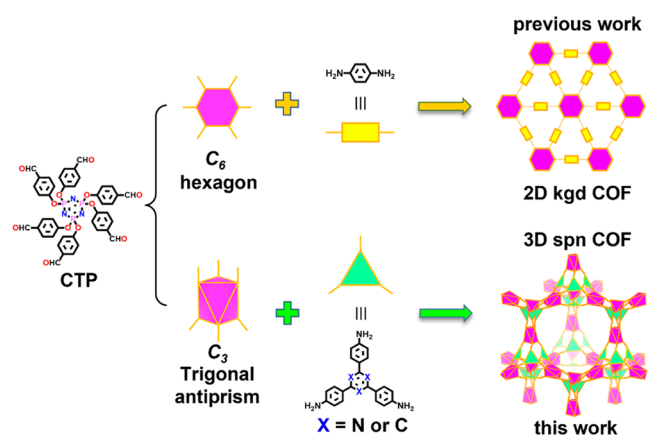
Herein, we report two 3D COFs denoted as TAA/TAB-CTP-COF with spn topology based on the trigonal antiprism (C₃) monomer hexa (4-formyl-phenoxy) cyclotriphosphazene (CTP) and planar amine linker monomers 2,4,6-tris(4-aminophenyl)-1,3,5-triazine (TAA) or 1,3,5-Tris (4-aminophenyl) benzene (TAB) (Scheme 1). The quasi-three-dimensional monomer CTP has a unique structure that can distort its 2D plane structure regularly.¹⁷ A planar unit with a C₆ configuration of CTP tends to form 2D COFs with kgd topology induced by a monomer with a C₂ configuration.³⁵ However, a 3D unit of trigonal antiprism (C₃) monomers of

CTP will be formed when the CTP twists excessively, which tends to form a 3D COF even connected with planar monomers. Besides, N, O, and P in the CTP can act as active sites, which is conducive to photocatalytic WOR, and the triazine structure of TAA can accept photogenerated electrons for ORR,^{36–39} thus forming a redox heteromotif molecular junction. Using water and oxygen as reactants, under light irradiation, efficient photocatalytic H₂O₂ production with a rate of 1041 $\mu\text{M h}^{-1}$ was achieved for TAA-CTP-COF without any photosensitizer and sacrificial agent. Furthermore, when isopropanol was used as a sacrificial agent, the rate of H₂O₂ generation increased to 2221 $\mu\text{M h}^{-1}$, which placed it among the highest reported photocatalytic crystalline materials. In addition, a series of experiments and theoretical calculations indicated that the TAA/TAB and CTP in TAA/TAB-CTP-COF formed a redox heteromotif molecular junction. Under illumination, the photogenerated electrons are transferred to TAA/TAB to achieve ORR, while holes are transferred to CTP to achieve WOR. Moreover, TAA-CTP-COF exhibits higher photoelectric response, better electron–hole separation ability, lower Gibbs free energy barrier, and higher photocatalytic performance for producing H₂O₂ compared to TAB-CTP-COF. This work expands the variety of 3D crystalline photocatalytic materials and is of great significance in the field of photocatalytic production of H₂O₂.

RESULTS AND DISCUSSION

Two 3D COFs were synthesized by coupling TAA or TAB with CTP through Schiff-base condensation by a solvothermal method in a mixed solvent of *o*-dichlorobenzene (*o*-DCB) and petroleum ether (PE) at 120 °C for 3 days (Figure 1a), denoted as TAA/TAB-CTP-COF, respectively. To elucidate the crystalline nature and gain a deep understanding of the structural information on TAA/TAB-CTP-COF, the crystal structure of TAA/TAB-CTP-COF was determined by powder X-ray diffraction (PXRD) combined with a theoretical structural simulation using the Materials Studio (Figures 1b and S1). The atomic coordinates of the crystal cells that made up TAA/TAB-CTP-COF are shown in Tables S1 and S2. For TAA-CTP-COF, the experimental PXRD pattern exhibited diffraction peaks at 1.95, 3.74, and 7.25°, which respectively corresponded to the (111), (311), and (602) facets. As revealed by the difference plot, with unweighted-profile *R* factor (*R*_p) = 5.5% and weighted-profile *R* factor (*R*_{wp}) = 7.2%. For TAB-CTP-COF, the experimental PXRD pattern exhibited diffraction peaks at 1.91, 3.75, and 7.24°, which showed results very similar to TAA-CTP-COF. This indicated that the two COFs had structural similarities and suggested the validity of the computational model. The formation of the Schiff-base linkages in TAA-CTP-COF was confirmed by solid-state ¹³C cross-polarization magic angle spinning (¹³C CP/MAS) NMR and Fourier transform infrared (FTIR) spectroscopies. The resonance signals at 158.9 ppm in the NMR spectra, as shown in Figure 1c, were characteristic of the carbons of C=N.⁴⁰ The nitrogen adsorption–desorption isotherms were measured at 77 K, and we can observe a sharp gas uptake at low relative pressures; the Brunauer–Emmett–Teller (BET) surface areas of TAA-CTP-COF and TAB-CTP-COF are 999.5 and 1075.2 m² g^{−1}, respectively (Figures S2–S3). In the FTIR spectrum, the peak at about 1625 cm^{−1} could be assigned to the C=N stretching vibration band of the resultant TAA/TAB-CTP-COF,⁴¹ while the C=O (–CHO) stretching vibration band at about 1700 cm^{−1} and the –NH₂ vibration band at about

Scheme 1. Schematic Representation of COFs with Different Topological Structures Synthesized by CTP



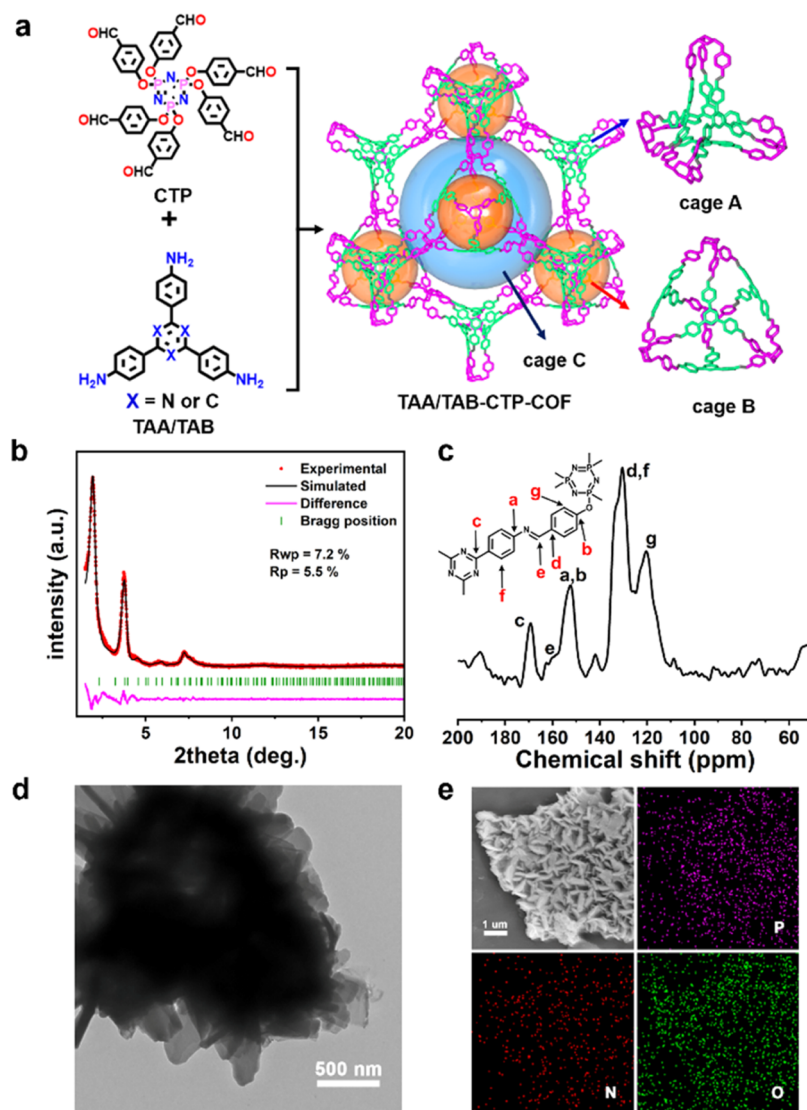


Figure 1. Structure and characterization of TAA/TAB-CTP-COF. (a) Schematic representation of the synthesis of TAA/TAB-CTP-COF. (b) Experimental (red dot) and simulated (black line) PXRD patterns of TAA-CTP-COF. (c) ^{13}C CP/MAS NMR spectrum of TAA-CTP-COF. (d) TEM image of TAA-CTP-COF. (e) SEM and elemental mapping images of TAA-CTP-COF.

3200–3500 cm^{-1} belonged to reactant monomers that reduced obviously (Figures S4–S5), which proved the successful synthesis of the Schiff-base structure. The existing elements were determined by X-ray photoelectron spectroscopy (XPS); in the XPS spectra of TAA/TAB-CTP-COF (Figures S6–S7), the four main peaks of TAA-CTP-COF with binding energies of 532.2, 398.4, 284.7, and 133.9 eV were ascribed to O 1s, N 1s, C 1s, and P 2p, respectively, which meant that C, N, O, and P elements were included in the structure. The N 1s spectrum showed that imine nitrogen ($-\text{C}=\text{N}-$, 399.2 eV) and nitrogen ($-\text{P}=\text{N}-$, 398.4 eV) bonds existed in TAA-CTP-COF, while the amino peak (≈ 400 eV) almost disappeared.¹⁷ This meant that the amino group was consumed after the condensation reaction, which was the same as the conclusions of FTIR spectroscopy. The fitted O 1s in XPS spectrum also demonstrated the presence of the P–O–C (533.6 eV) bonds.

The structural features of TAA/TAB-CTP-COF could be concluded based on the above characterizations and theoretical structure (Figure 1a). In these COFs, each building unit of CTP was connected to six TAA/TAB units, and each TAA/

TAB unit was covalently connected to three building units of CTP. The CTP building units with twisting structures were arranged directionally and connected with TAA/TAB to form two types of tetrahedral cages (cage A and cage B). Both of them were composed of four TAA/TAB building units and four CTP building units. Cage A had a radius of about 2 Å with shrink formation, and cage B formed a much larger cavity with a radius of approximately 8 Å with expanded formation. Cage C was composed of six units of cage A and four units of cage B (Figure S8). Cage A and cage B were connected with CTP as their vertex and TAA/TAB as their face.

Different from the structure of the traditional spn topology, TAA/TAB-CTP-COF consisted of one large and one small tetrahedron instead of a uniform and regular tetrahedral cage (Figure S9). We could simplify cage A and cage B into a small tetrahedron (dark blue) and a large tetrahedron (muddy yellow). Besides, the TAA/TAB-CTP-COF cage had a special structure with spn topology comprised of a large channel and a small channel from the tile diagram, which was different from the traditional dia topology with regular and uniform channels (Figure S10). Because of the distinctive nature of this type of

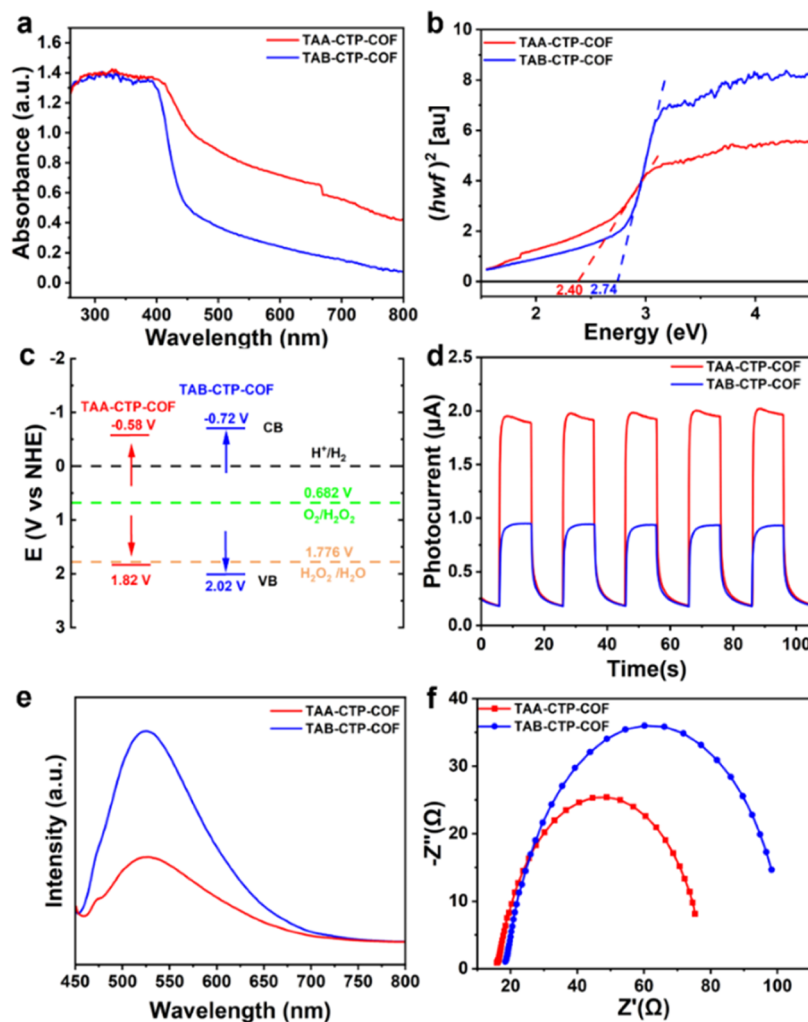


Figure 2. Characterizations of the optical properties for TAA/TAB-CTP-COF. (a) UV–vis absorption spectra. (b) Tauc plot for bandgap calculation. (c) Band-structure diagram. (d) Transient photocurrent response. (e) Steady-state photoluminescence (PL) measurements. (f) Nyquist plots of TAA/TAB-CTP-COF.

structure, as illustrated in Figure S11, we could observe that the TAA/TAB-CTP-COF cage was comprised of a two-layered structure (blue represents the inner layer and red represents the outer layer). The morphological characteristics of TAA/TAB-CTP-COF were visualized by transmission electron microscopy (TEM) and scanning electron microscopy (SEM). As shown in Figures 1d and S12, the results indicated that TAA/TAB-CTP-COFs were composed of 1–2 μm schistose objects. In the high-resolution TEM (HR-TEM) images of TAA-CTP-COF (Figure S13), oriented lattice fringes of TAA-CTP-COF were observed, which confirmed that the synthesized TAA-CTP-COF had high crystallinity. In Figure 1e, the morphology of COFs exhibited accumulated nanosheets, and energy-dispersive (EDS) element mapping images showed that P, N, and O atoms were uniformly distributed throughout the TAA-CTP-COF. Figure S14 shows that TAB-CTP-COF had a similar morphology.

Stability was an important factor to measure the performance of crystalline porous materials. The chemical stability was determined by soaking TAA-CTP-COF in different solutions (H_2O , methanol (CH_3OH), acetonitrile (CH_3CN), and N,N -dimethylformamide (DMF)) for more than 48 h, and then tested by PXRD and FTIR spectroscopy. Compared with PXRD before and after the experiment (Figure S15), the

crystallinity of the material did not show an obvious change. The FTIR spectrum further proved that the chemical structure of TAA-CTP-COF was retained after soaking in these solutions (Figure S16). To characterize the thermal stability of these materials, thermogravimetric analysis (TGA) was conducted in an O_2 atmosphere, which indicated that both of them were thermally stable up to about 400 $^\circ\text{C}$ (Figure S17).

Based on the synthesized COFs mentioned above, we further tested their photophysical properties. As shown in the ultraviolet and visible (UV–vis) absorption spectra, both of the TAA/TAB-CTP-COFs possessed a broad visible light absorption range at 400–800 nm (Figure 2a), but the visible light absorption intensity of TAA-CTP-COF was higher than that of TAB-CTP-COF, which meant that TAA-CTP-COF had stronger visible light response than TAB-CTP-COF. Furthermore, through their Tauc plots, the bandgap (E_g) values of TAA/TAB-CTP-COF were 2.40 and 2.74 eV, which represented their semiconductor characteristics (Figure 2b). In order to determine their energy band positions, the Mott–Schottky (MS) electrochemical measurement was carried out for TAA/TAB-CTP-COF, according to the MS plots (Figures S18–S19). The conduction band (CB) positions of TAA/TAB-CTP-COF were calculated as -0.58 and -0.72 V (vs NHE, pH = 7). Combined with the band gap of TAA/TAB-

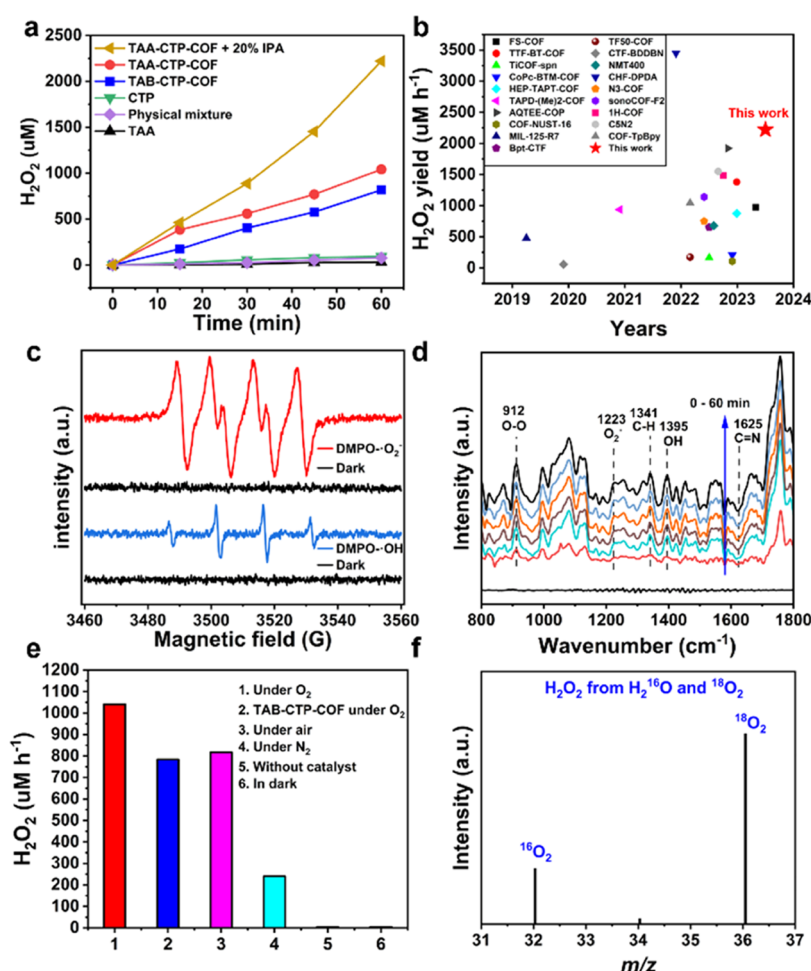


Figure 3. Performance of photosynthesized H₂O₂ for TAA/TAB-CTP-COF. (a) Photocatalytic activities of TAA/TAB-CTP-COF, TAA, CTP, and their physical mixture for H₂O₂ production in pure water and O₂ atmosphere. (b) Comparison of the reported photocatalytic H₂O₂ production. (c) EPR signals of the reaction solution in the dark and under light illumination in the presence of DMPO as the spin-trapping reagent of TAA-CTP-COF. (d) DRIFTS spectrum of TAA-CTP-COF in H₂O₂ photosynthesis. (e) Photocatalytic H₂O₂ production under various conditions of TAA-CTP-COF. (f) ¹⁸O₂ isotope experiment of TAA-CTP-COF to explore the source of H₂O₂.

CTP-COF, which was calculated from the Tauc plots, their valence band (VB) positions were 1.82 and 2.02 V (vs NHE, pH = 7), respectively. Thus, TAA/TAB-CTP-COF could realize WOR and ORR.

To further understand the light absorption performances of TAA, TAB, and CTP, UV-vis absorption spectroscopy was conducted. On comparing the absorption spectra across the entire range, it was obvious that TAA had a stronger absorption intensity than TAB in the full spectrum (Figures S20 and S21), which confirmed that the structure of triazine showed better light absorption. An MS electrochemical measurement experiment was also performed to locate the conduction bands of TAA, TAB, and CTP to verify the accuracy of the above results (Figure S22). The results demonstrated that the CB positions of TAA, TAB, and CTP were −0.40, −0.95, and −0.58 V, respectively. Combined with the UV-vis absorption data of TAA, TAB, and CTP, their VB positions were 2.45, 2.50, and 2.32 V (Figure S23), respectively, which showed that TAA, TAB, and CTP could all complete WOR and ORR. What's more, the theoretical redox potentials of H₂O₂ from O₂ ($E_{\text{H}_2\text{O}_2/\text{O}_2} = 0.68$ V vs NHE) and H₂O ($E_{\text{H}_2\text{O}_2/\text{H}_2\text{O}} = 1.76$ V vs NHE) were met by the band structures of TAA/TAB-CTP-COF (Figure 2c), which meant

that both of the COFs were able to effectively realize the full reaction photosynthesis of H₂O₂ theoretically.²⁵ The above experiment indicated that not only did the photocatalysis of the two types of COFs go through the ORR pathway, but they also showed synergistic photocatalytic activity through the WOR route.

The photocurrent density of TAA-CTP-COF was significantly higher than that of TAB-CTP-COF, which indicated that the TAA-CTP-COF had more usable surface carriers and higher charge separation efficiency (Figure 2d).⁴² Through photoluminescence (PL) measurements, the charge-transfer behaviors were studied. In Figure 2e, it was obvious that the PL intensity of TAA-CTP-COF was lower than that of TAB-CTP-COF; their excitation wavelengths were both at 525 nm. Combined with the transient photocurrent response, TAA-CTP-COF had a better ability for electron-hole separation and photocatalysis than TAB-CTP-COF. By comparing the electrochemical impedance spectra (EIS) of TAA/TAB-CTP-COF, it was found that the semi-cycle arc radius of the Nyquist plot in TAA-CTP-COF was smaller than that of TAB-CTP-COF, which indicated the fast interfacial charge transfer in TAA-CTP-COF,⁴³ thus improving the separation efficiency of photogenerated electrons and holes (Figure 2f).

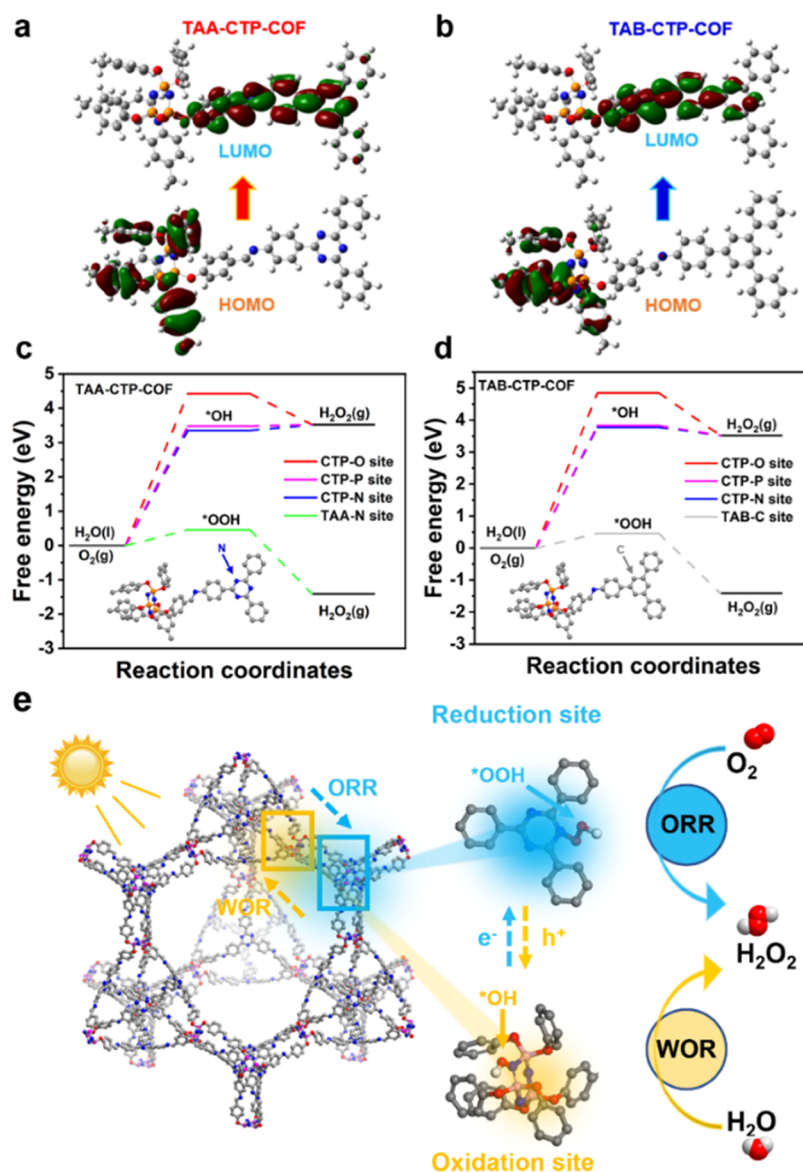


Figure 4. DFT calculations and the proposed reaction mechanism. The distribution of HOMO and LUMO wave functions of (a) TAA-CTP-COF and (b) TAB-CTP-COF in real space. Free energy diagrams of (c) TAA-CTP-COF and (d) TAB-CTP-COF for the photosynthesis of H_2O_2 through the WOR and ORR pathways. (e) Adsorption configuration of $^*\text{OH}$ on CTP and $^*\text{OOH}$ on TAA of the TAA-CTP-COF.

Based on the above experimental results of photophysical characterization, we further explored their photocatalytic performance for H_2O_2 production. Under the condition of pure water solution (no additional sacrificial agent) in an oxygen atmosphere, we carried out the photosynthesis experiment of H_2O_2 ; the cerium sulfate colorimetric method and titanium oxysulfate colorimetric method were used for determining the yield, and a detailed experimental description is provided in the Supporting Information (Figures S24–S27). Based on the photocatalytic performances of TAA-CTP-COF, TAB-CTP-COF, TAA, CTP, and the physical mixture of TAA and CTP shown in Figure 3a, the H_2O_2 production showed an obvious linear relationship with reaction time. With regard to the H_2O_2 production rate, the H_2O_2 yield of TAA-CTP-COF gradually increased and finally reached $1041 \mu\text{M h}^{-1}$, which was about 1.3 times higher than that of TAB-CTP-COF ($818 \mu\text{M h}^{-1}$) without any additives. To further demonstrate the superiority of TAA-CTP-COF, we tested the performance of TAA-CTP-COF in the presence of the sacrificial agent

isopropanol (IPA); the yield of H_2O_2 in TAA-CTP-COF reached $2221 \mu\text{M h}^{-1}$ when the volume fraction of isopropanol in water was 20%. The photocatalytic performance of TAA-CTP-COF could reach the level of most reported materials (Figure 3b and Table S3). In addition, from the performances of TAA, CTP, and their physical mixture, the H_2O_2 production rates for TAA, CTP, and their physical mixture were 30, 93, and $77 \mu\text{M h}^{-1}$, respectively, under light irradiation, which was much lower than that of TAA-CTP-COF, further confirming the superiority of the covalent connection molecular junction in TAA-CTP-COF. To prove the catalytic stability of materials, the cyclic stability of TAA-CTP-COF was investigated (Figure S28). After three repeated cycles of photocatalytic tests, the production rate of H_2O_2 did not show a significant decrease. To investigate the effect of pH on the yield of H_2O_2 , we conducted photocatalytic tests under different pH conditions. It can be seen that the yield under acidic conditions is higher than that under alkaline conditions, and its performance decreases with an increase in acidity or alkalinity (Figure S29).

In addition, we also tested the H_2O_2 yield at different reaction scales (Figure S30). Additional support for stability came from the negligible structural change of TAA-CTP-COF after the test according to the FTIR spectroscopy, XPS, and PXRD measurements (Figures S31–S33). In the FTIR spectrum, the $\text{C}\equiv\text{N}$ stretching vibration at 1625 cm^{-1} still existed in TAA-CTP-COF after the test. In the XPS spectra before and after the reaction, it could also be seen that the binding energies of the four main peaks of C 1s, N 1s, O 1s, and P 2p were basically unchanged. The PXRD test also confirmed the integrity of the TAA-CTP-COF structure after the experiment. In addition, to test the stability of the material under photoirradiation, we characterized the material after long-term photoirradiation for 12 and 24 h. PXRD, FTIR spectroscopy, SEM, and TEM (Figures S34–S37) studies showed that the material still maintained stability. The above data showed that the catalytic structure of TAA-CTP-COF was stable, indicating that the material could be recycled for continuous H_2O_2 production.

To investigate the reaction mechanism of photosynthesis of H_2O_2 by TAA/TAB-CTP-COF, electron paramagnetic resonance (EPR) spectroscopy was conducted by using 5,5-dimethyl-1-pyrroline *N*-oxide (DMPO) as the spin-trap agent (Figures 3c and S38).⁴⁴ Under light irradiation, the typical six and four characteristic signals for $\text{DMPO}\cdot\text{O}_2^-$ and $\text{DMPO}\cdot\text{OH}$ were distinctly observed in TAA/TAB-CTP-COF. However, no signals were detected in the dark conditions, which indicated that the single-electron reduction of O_2 to $\cdot\text{OOH}$ as a reaction intermediate and the intermediate species of $\cdot\text{OH}$ were generated during the process of illumination.²⁵ Compared with TAB-CTP-COF, the EPR signal of TAA-CTP-COF was slightly stronger, indicating that triazine had a promoting effect on the production of $\cdot\text{OOH}$ and $\cdot\text{OH}$ intermediates overall. Based on the above experiments, we concluded that $\cdot\text{OOH}$ and $\cdot\text{OH}$ participated in the generation of H_2O_2 during the photoreaction process. In addition, through the in situ diffuse reflectance infrared Fourier transform spectroscopy (DRIFTS) measurements (Figure 3d), TAA-CTP-COF displayed relatively obvious infrared absorption peaks at 912, 1395, and 1625 cm^{-1} , which were attributed to $\text{O}-\text{O}$, OH , and $\text{C}\equiv\text{N}$ absorption, respectively. These results indicated that $\cdot\text{OOH}$ and $\cdot\text{OH}$ were key intermediates in the process of photocatalytic generation of H_2O_2 . The above experiment further indicated that the photocatalytic mechanism of H_2O_2 generation consisted of both ORR and WOR mechanisms.

As a comparison, when the control experiment was performed either in the dark or in the absence of TAA/TAB-CTP-COF, no H_2O_2 was generated. Furthermore, the photocatalytic H_2O_2 generation of TAA-CTP-COF under various atmospheric conditions was also measured. The highest H_2O_2 production rate of $1041\text{ }\mu\text{M h}^{-1}$ was achieved under O_2 atmosphere, which decreased to $784\text{ }\mu\text{M h}^{-1}$ in air and to $241\text{ }\mu\text{M h}^{-1}$ in N_2 conditions (Figure 3e), suggesting that the formation of H_2O_2 was predominantly through the reduction of oxygen, while the remaining part was through the oxidation of water. In addition, almost no oxygen could be measured from the WOR half-reaction with NaIO_3 as the e^- -trapping agent in a N_2 atmosphere (Figure S39), which indicated that the 4e^- oxidation of water to oxygen did not occur. We also carried out isotope-labeling experiments on TAA-CTP-COF to ascertain the WOR and ORR processes (Figure 3f); we could thus learn that TAA-CTP-COF

underwent simultaneous ORR and WOR during the photocatalytic process. The stronger peak of $^{18}\text{O}_2$ in the mass spectrum suggested that the process of photocatalytic generation of H_2O_2 occurred mainly through ORR, which was consistent with the data observed in EPR testing.

Based on the density functional theory (DFT) calculations, we calculated the highest occupied molecular orbital (HOMO) and lowest-unoccupied molecular orbital (LUMO) energy level distributions of TAA/TAB-CTP-COF under light excitation. As can be seen from Figure 4a,b, TAA/TAB-CTP-COF presented excellent spatial charge separation. The HOMO level was distributed on the CTP unit, while the LUMO level was distributed on the TAA/TAB unit. The energy level calculation results suggested that, in the reaction process, the oxidation process (H_2O oxidation to H_2O_2) occurred in the CTP unit, and the reduction process (O_2 reduction to H_2O_2) occurred in the TAA/TAB unit of TAA/TAB-CTP-COF.

In addition, we calculated the possible photocatalytic active sites and the Gibbs free energy changes of generating $\cdot\text{OH}$ and $\cdot\text{OOH}$ intermediates for TAA/TAB-CTP-COF during WOR and ORR to form H_2O_2 , respectively (Figure 4c,d). For the WOR of TAA/TAB-CTP-COF, the energy barrier for H_2O -to- $\cdot\text{OH}$ on the O site was the highest, at 4.43 and 4.85 eV, respectively. This suggested that the O element was not the most effective active site for the WOR process. However, N and P as active sites for H_2O -to- $\cdot\text{OH}$ exhibit lower energy barriers of 3.35 and 3.48 eV in TAA-CTP-COF, respectively. On the other hand, the energy barriers of N and P sites for H_2O -to- $\cdot\text{OH}$ were 3.78 and 3.83 eV in TAB-CTP-COF, respectively. This suggested that the N site in CTP could be the most active site in the photocatalytic WOR process to H_2O_2 (Figure S40). It was worth noting that according to the free energy diagram, the free energy of the N site and the P site for H_2O -to- $\cdot\text{OH}$ in CTP was close, which illustrated that P could also be the active site for generating $\cdot\text{OH}$ during the photocatalytic process.

From the above results, TAA-CTP-COF had more advantages in photocatalytic WOR than TAB-CTP-COF. For the ORR of TAA/TAB-CTP-COF, it was obvious that the energy barrier for O_2 -to- $\cdot\text{OOH}$ of the N site on the triazine position on the TAA building unit was lower than that of the C site on the TAB (Figure S41). Compared with the energy barrier value of TAB-CTP-COF (0.46 eV for O_2 -to- $\cdot\text{OOH}$), the energy barrier for O_2 -to- $\cdot\text{OOH}$ of TAA-CTP-COF was 0.34 eV, indicating the positive influence of TAA units on reducing the energy barrier of ORR and that TAA-CTP-COF was superior to TAB-CTP-COF in the photocatalytic ORR process.

Based on the above experimental and computational results, a favorable catalytic mechanism for the photocatalytic production of H_2O_2 using TAA/TAB-CTP-COF was proposed (Figure 4e). Under light irradiation, when TAA/TAB-CTP-COF absorbed photons, the photoinduced electrons underwent fast transfer from the CTP (HOMO) to TAA/TAB (LUMO). Subsequently, O_2 was converted into the active intermediate $\cdot\text{OOH}$ by acquiring electrons from TAA/TAB. Meanwhile, due to the separation of electrons and holes, the holes could be utilized by H_2O to form $\cdot\text{OH}$ intermediates. Subsequently, $\cdot\text{OH}$ and $\cdot\text{OOH}$ underwent further oxidation and reduction on TAA/TAB-CTP-COF to generate H_2O_2 , respectively. Furthermore, the experimental results showed that TAA-CTP-COF exhibited higher activity than TAB-CTP-

COF, which can be attributed to the following reasons: (1) In the UV–vis adsorption spectrum, PL spectrum, and transient photocurrent response measurements, TAA-CTP-COF exhibited higher photoelectric response and electron–hole separation efficiency than TAB-CTP-COF because TAA acts as a stronger electron acceptor. (2) The free energy barrier of the rate-determining step for O₂ reduction on the TAA site of TAA-CTP-COF was lower than that on the TAB site of TAB-CTP-COF, indicating that the strong electron-withdrawing ability of the TAA unit represented higher activity. All of these results reflected the fact that the combination of suitable redox ability, photophysical properties, optoelectronic behavior, and synergistic effect between functional groups determined the photocatalytic performance of a COF catalyst, which was successfully achieved in the rationally designed TAA-CTP-COF.

CONCLUSIONS

In summary, we designed and synthesized two 3D COFs with spn topology using a flexible phosphoronitrile building block (CTP) combined with two triangular construction units (TAA/TAB). It is worth noting that the resulting TAA-CTP-COF exhibits high crystallinity, abundant catalytic active sites, and excellent photocatalytic stability for photocatalytic H₂O₂ production. The redox heteromorph molecular junction formed in TAA-CTP-COF results in the effective transfer of electrons from the CTP to the TAA under light irradiation and achieves WOR on CTP and ORR on TAA for H₂O₂ production. Especially, TAA-CTP-COF can effectively generate H₂O₂ through photocatalysis without the need for any photosensitizers, organic scavengers, or cocatalysts. The optimal generation rate observed is 1041 μM h^{−1} for TAA-CTP-COF. Furthermore, under the conditions of isopropanol as a sacrificial agent, the generation rate of H₂O₂ is 2221 μM h^{−1}, achieving the yield level of most materials. This approach offers an efficient solution for H₂O₂ generation and has the potential for a wide range of applications. This work presents a new strategy for the development of 3D COF synthetic materials and highlights their potential as oxidation–reduction heteromorph molecular junctions in solar energy conversion, which also emphasizes the importance of 3D COFs in this field.

ASSOCIATED CONTENT

Supporting Information

The Supporting Information is available free of charge at <https://pubs.acs.org/doi/10.1021/acscatal.3c06078>.

Detailed information regarding the experimental methods; characterization analysis; DFT calculations; and simulation of the theoretical COF structure (PDF)

AUTHOR INFORMATION

Corresponding Authors

Meng Lu – School of Chemistry, South China Normal University, Guangzhou, Guangdong 510006, P. R. China; orcid.org/0000-0003-4502-7517; Email: menglul@scnu.edu.cn

Ya-Qian Lan – School of Chemistry, South China Normal University, Guangzhou, Guangdong 510006, P. R. China; orcid.org/0000-0002-2140-7980; Email: yqlan@scnu.edu.cn

Authors

Jia-Peng Liao – School of Chemistry, South China Normal University, Guangzhou, Guangdong 510006, P. R. China

Mi Zhang – School of Chemistry, South China Normal University, Guangzhou, Guangdong 510006, P. R. China

Pei Huang – School of Chemistry, South China Normal University, Guangzhou, Guangdong 510006, P. R. China

Long-Zhang Dong – School of Chemistry, South China Normal University, Guangzhou, Guangdong 510006, P. R. China; orcid.org/0000-0002-9276-5101

Tian-Tian Ma – School of Chemistry, South China Normal University, Guangzhou, Guangdong 510006, P. R. China

Guo-Zhang Huang – Department of Chemistry, Guangdong Provincial Key Laboratory of Catalytic Chemistry, Southern University of Science and Technology, Shenzhen, Guangdong 518055, P. R. China; orcid.org/0000-0001-9167-0090

Yu-Fei Liu – School of Chemistry, South China Normal University, Guangzhou, Guangdong 510006, P. R. China

Shun-Li Li – School of Chemistry, South China Normal University, Guangzhou, Guangdong 510006, P. R. China

Complete contact information is available at: <https://pubs.acs.org/doi/10.1021/acscatal.3c06078>

Author Contributions

[§]J.-P.L. and M.Z. contributed equally to this work.

Notes

The authors declare no competing financial interest.

ACKNOWLEDGMENTS

This work was financially supported by the National Key R&D Program of China (2023YFA1507204), NSFC (Nos. 22225109, 22071109, 22105080, and 22201083), the China National Postdoctoral Program for Innovative Talents (BX20220115), the Project funded by China Postdoctoral Science Foundation (Nos. 2021M701270 and 2020M682748), the Guangdong Basic and Applied Basic Research Foundation (2023A1515010779 and 2023A1515010928), and the Guangzhou Basic and Applied Basic Research Fund Project (No. 202102020209).

REFERENCES

- (1) Chen, X.; Geng, K.; Liu, R.; Tan, K. T.; Gong, Y.; Li, Z.; Tao, S.; Jiang, Q.; Jiang, D. Covalent organic frameworks: chemical approaches to designer structures and built-in functions. *Angew. Chem., Int. Ed.* **2020**, *59* (13), 5050–5091.
- (2) Lu, M.; Zhang, M.; Liu, J.; Chen, Y.; Liao, J.-P.; Yang, M.-Y.; Cai, Y.-P.; Li, S.-L.; Lan, Y.-Q. Covalent organic framework based functional materials: important catalysts for efficient CO₂ utilization. *Angew. Chem., Int. Ed.* **2022**, *61* (15), No. e202200003.
- (3) Diercks, C. S.; Yaghi, O. M. The atom, the molecule, and the covalent organic framework. *Science* **2017**, *355* (6328), No. eaal1585.
- (4) Yu, C.; Li, H.; Wang, Y.; Suo, J.; Guan, X.; Wang, R.; Valtchev, V.; Yan, Y.; Qiu, S.; Fang, Q. Three-dimensional triptycene-functionalized covalent organic frameworks with hea net for hydrogen adsorption. *Angew. Chem., Int. Ed.* **2022**, *61* (13), No. e202117101.
- (5) Guan, X.; Chen, F.; Fang, Q.; Qiu, S. Design and applications of three dimensional covalent organic frameworks. *Chem. Soc. Rev.* **2020**, *49* (5), 1357–1384.
- (6) Gropp, C.; Ma, T.; Hanikel, N.; Yaghi, O. M. Design of higher valency in covalent organic frameworks. *Science* **2020**, *370* (6515), No. eabd6406.
- (7) Jin, F.; Lin, E.; Wang, T.; Yan, D.; Yang, Y.; Chen, Y.; Cheng, P.; Zhang, Z. Rationally fabricating 3D porphyrinic covalent organic

frameworks with scu topology as highly efficient photocatalysts. *Chem* **2022**, *8* (11), 3064–3080.

- (8) Chen, L.; Gong, C.; Wang, X.; Dai, F.; Huang, M.; Wu, X.; Lu, C.-Z.; Peng, Y. Substoichiometric 3D covalent organic frameworks based on hexagonal linkers. *J. Am. Chem. Soc.* **2021**, *143* (27), 10243–10249.
- (9) Jin, F.; Lin, E.; Wang, T.; Geng, S.; Wang, T.; Liu, W.; Xiong, F.; Wang, Z.; Chen, Y.; Cheng, P.; Zhang, Z. Bottom-up synthesis of 8-Connected three-dimensional covalent organic frameworks for highly efficient ethylene/ethane separation. *J. Am. Chem. Soc.* **2022**, *144* (12), 5643–5652.
- (10) Gui, B.; Lin, G.; Ding, H.; Gao, C.; Mal, A.; Wang, C. Three-dimensional covalent organic frameworks: from topology design to applications. *Acc. Chem. Res.* **2020**, *53* (10), 2225–2234.
- (11) Kandambeth, S.; Dey, K.; Banerjee, R. Covalent organic frameworks: Chemistry beyond the structure. *J. Am. Chem. Soc.* **2019**, *141* (5), 1807–1822.
- (12) Li, Z.; Sheng, L.; Wang, H.; Wang, X.; Li, M.; Xu, Y.; Cui, H.; Zhang, H.; Liang, H.; Xu, H.; He, X. Three-dimensional covalent organic framework with ceq topology. *J. Am. Chem. Soc.* **2021**, *143* (1), 92–96.
- (13) Li, H.; Ding, J.; Guan, X.; Chen, F.; Li, C.; Zhu, L.; Xue, M.; Yuan, D.; Valtchev, V.; Yan, Y.; Qiu, S.; Fang, Q. Three-dimensional large-pore covalent organic framework with stp topology. *J. Am. Chem. Soc.* **2020**, *142* (31), 13334–13338.
- (14) Li, H.; Chen, F.; Guan, X.; Li, J.; Li, C.; Tang, B.; Valtchev, V.; Yan, Y.; Qiu, S.; Fang, Q. Three-dimensional triptycene-based covalent organic frameworks with ceq or acs topology. *J. Am. Chem. Soc.* **2021**, *143* (7), 2654–2659.
- (15) Liu, X. L.; Li, J.; Gui, B.; Lin, G. Q.; Fu, Q.; Yin, S.; Liu, X. F.; Sun, J. L.; Wang, C. A crystalline three-dimensional covalent organic framework with flexible building blocks. *J. Am. Chem. Soc.* **2021**, *143* (4), 2123–2129.
- (16) Li, X.; Jia, Z.; Zhang, J.; He, N.; Long, H.; Qi, Y.; Li, J.; Liu, N.; Li, Y.; Ma, L. Construction of covalent organic frameworks with alternating rigid and flexible units and their controlled release of active sites. *Chem. Eng. J.* **2023**, *454*, No. 140119.
- (17) Guo, X.; Li, Y.; Zhang, M.; Cao, K.; Tian, Y.; Qi, Y.; Li, S.; Li, K.; Yu, X.; Ma, L. Colyliform crystalline 2D covalent organic frameworks (COFs) with quasi-3D topologies for rapid I₂ adsorption. *Angew. Chem., Int. Ed.* **2020**, *59* (50), 22697–22705.
- (18) Gui, B.; Xin, J.; Cheng, Y.; Zhang, Y.; Lin, G.; Chen, P.; Ma, J. X.; Zhou, X.; Sun, J.; Wang, C. Crystallization of dimensional Isomers in covalent organic frameworks. *J. Am. Chem. Soc.* **2023**, *145* (20), 11276–11281.
- (19) Chen, B.; Dong, M.; Liu, S.; Xie, Z.; Yang, J.; Li, S.; Wang, Y.; Du, J.; Liu, H.; Han, B. CO₂ Hydrogenation to formate catalyzed by Ru coordinated with a N,P-containing polymer. *ACS Catal.* **2020**, *10* (15), 8557–8566.
- (20) Guo, S.; Zhang, H.; Chen, Y.; Liu, Z.; Yu, B.; Zhao, Y.; Yang, Z.; Han, B.; Liu, Z. Visible-light-driven photoreduction of CO₂ to CH₄ over N,O,P-containing covalent organic polymer submicro-spheres. *ACS Catal.* **2018**, *8* (5), 4576–4581.
- (21) Ma, T. Y.; Ran, J.; Dai, S.; Jaroniec, M.; Qiao, S. Z. Phosphorus-doped graphitic carbon nitrides grown in situ on carbon-fiber paper: flexible and reversible oxygen electrodes. *Angew. Chem., Int. Ed.* **2015**, *54* (15), 4646–4650.
- (22) Zhang, Y.; Antonietti, M. Photocurrent generation by polymeric carbon nitride solids: an initial step towards a novel photovoltaic system. *Chem. - Asian J.* **2010**, *5* (6), 1307–1311.
- (23) Xu, X.; Sa, R.; Huang, W.; Sui, Y.; Chen, W.; Zhou, G.; Li, X.; Li, Y.; Zhong, H. Conjugated organic polymers with anthraquinone redox centers for efficient photocatalytic hydrogen peroxide production from water and oxygen under visible light irradiation without any additives. *ACS Catal.* **2022**, *12* (20), 12954–12963.
- (24) Li, L.; Xu, L.; Hu, Z.; Yu, J. C. Enhanced mass transfer of oxygen through a gas–liquid–solid interface for photocatalytic hydrogen peroxide production. *Adv. Funct. Mater.* **2021**, *31* (52), No. 2106120, DOI: 10.1002/adfm.202106120.
- (25) Chang, J. N.; Li, Q.; Shi, J. W.; Zhang, M.; Zhang, L.; Li, S.; Chen, Y.; Li, S. L.; Lan, Y. Q. Oxidation-reduction molecular junction covalent organic frameworks for full reaction photosynthesis of H₂O₂. *Angew. Chem., Int. Ed.* **2022**, *62* (9), No. e202218868.
- (26) Chen, D.; Chen, W.; Wu, Y.; Wang, L.; Wu, X.; Xu, H.; Chen, L. Covalent organic frameworks containing dual O₂ reduction centers for overall photosynthetic hydrogen peroxide production. *Angew. Chem., Int. Ed.* **2022**, *62* (9), No. e202217479.
- (27) Chai, S.; Chen, X.; Zhang, X.; Fang, Y.; Sprick, R. S.; Chen, X. Rational design of covalent organic frameworks for efficient photocatalytic hydrogen peroxide production. *Environ. Sci.: Nano* **2022**, *9* (7), 2464–2469.
- (28) Krishnaraj, C.; Jena, H. S.; Bourda, L.; Laemont, A.; Pachfule, P.; Roeser, J.; Chandran, C. V.; Borgmans, S.; Rogge, S. M. J.; Leus, K.; Stevens, C. V.; Martens, J. A.; Van Speybroeck, V.; Breynaert, E.; Thomas, A.; Van Der Voort, P. Strongly reducing (diarylamino) benzene-based covalent organic framework for metal-free visible light photocatalytic H₂O₂ generation. *J. Am. Chem. Soc.* **2020**, *142* (47), 20107–20116.
- (29) Zhao, W.; Yan, P.; Li, B.; Bahri, M.; Liu, L.; Zhou, X.; Clowes, R.; Browning, N. D.; Wu, Y.; Ward, J. W.; Cooper, A. I. Accelerated synthesis and discovery of covalent organic framework photocatalysts for hydrogen peroxide production. *J. Am. Chem. Soc.* **2022**, *144* (22), 9902–9909.
- (30) Hu, H.; Tao, Y.; Wang, D.; Li, C.; Jiang, Q.; Shi, Y.; Wang, J.; Qin, J.; Zhou, S.; Kong, Y. Rational modification of hydroxy-functionalized covalent organic frameworks for enhanced photocatalytic hydrogen peroxide evolution. *J. Colloid Interface Sci.* **2023**, *629*, 750–762.
- (31) Liu, F.; Zhou, P.; Hou, Y.; Tan, H.; Liang, Y.; Liang, J.; Zhang, Q.; Guo, S.; Tong, M.; Ni, J. Covalent organic frameworks for direct photosynthesis of hydrogen peroxide from water, air and sunlight. *Nat. Commun.* **2023**, *14* (1), No. 4344.
- (32) McKee, D. W. Catalytic decomposition of hydrogen peroxide by metals and alloys of the platinum group. *J. Catal.* **1969**, *14* (4), 355–364.
- (33) Wu, M.; Shan, Z.; Wang, J.; Liu, T.; Zhang, G. Three-dimensional covalent organic framework with tty topology for enhanced photocatalytic hydrogen peroxide production. *Chem. Eng. J.* **2023**, *454*, No. 140121.
- (34) Zhang, L.; Li, R. H.; Li, X. X.; Liu, J.; Guan, W.; Dong, L. Z.; Li, S. L.; Lan, Y. Q. Molecular oxidation-reduction junctions for artificial photosynthetic overall reaction. *Proc. Natl. Acad. Sci. U.S.A.* **2022**, *119* (40), No. e2210550119.
- (35) Li, L.; Yun, Q.; Zhu, C.; Sheng, G.; Guo, J.; Chen, B.; Zhao, M.; Zhang, Z.; Lai, Z.; Zhang, X.; Peng, Y.; Zhu, Y.; Zhang, H. Isorecticular series of two-dimensional covalent organic frameworks with the kgd topology and controllable micropores. *J. Am. Chem. Soc.* **2022**, *144* (14), 6475–6482.
- (36) Chen, L.; Wang, L.; Wan, Y.; Zhang, Y.; Qi, Z.; Wu, X.; Xu, H. Acetylene and diacetylene functionalized covalent triazine frameworks as metal-free photocatalysts for hydrogen peroxide production: A new two-electron water oxidation pathway. *Adv. Mater.* **2020**, *32* (2), No. 1904433.
- (37) Cheng, H.; Lv, H.; Cheng, J.; Wang, L.; Wu, X.; Xu, H. Rational design of covalent heptazine frameworks with spatially separated redox centers for high-efficiency photocatalytic hydrogen peroxide production. *Adv. Mater.* **2022**, *34* (7), No. 2107480.
- (38) Wu, C.; Teng, Z.; Yang, C.; Chen, F.; Yang, H. B.; Wang, L.; Xu, H.; Liu, B.; Zheng, G.; Han, Q. Polarization engineering of covalent triazine frameworks for highly efficient photosynthesis of hydrogen peroxide from molecular oxygen and water. *Adv. Mater.* **2022**, *34* (28), No. 2110266.
- (39) Ma, J.; Peng, X.; Zhou, Z.; Yang, H.; Wu, K.; Fang, Z.; Han, D.; Fang, Y.; Liu, S.; Shen, Y.; Zhang, Y. Extended conjugation refining carbon nitride for non-sacrificial H₂O₂ photosynthesis and hypoxic tumor therapy. *Angew. Chem., Int. Ed.* **2022**, *61* (43), No. e202210856.

(40) Chang, J.; Li, C.; Wang, X.; Li, D.; Zhang, J.; Yu, X.; Li, H.; Yao, X.; Valtchev, V.; Qiu, S.; Fang, Q. Quasi-three-dimensional cyclotriphosphazene-based covalent organic framework nanosheet for efficient oxygen reduction. *Nano-Micro Lett.* **2023**, *15* (1), No. 159.

(41) Zhou, J.; Li, J.; Kan, L.; Zhang, L.; Huang, Q.; Yan, Y.; Chen, Y.; Liu, J.; Li, S. L.; Lan, Y. Q. Linking oxidative and reductive clusters to prepare crystalline porous catalysts for photocatalytic CO₂ reduction with H₂O. *Nat. Commun.* **2022**, *13* (1), No. 4681.

(42) Zhang, M.; Lu, M.; Lang, Z. L.; Liu, J.; Liu, M.; Chang, J. N.; Li, L. Y.; Shang, L. J.; Wang, M.; Li, S. L.; Lan, Y. Q. Semiconductor/covalent-organic-framework Z-scheme heterojunctions for artificial photosynthesis. *Angew. Chem., Int. Ed.* **2020**, *59* (16), 6500–6506.

(43) Chang, J.-N.; Li, Q.; Yan, Y.; Shi, J.-W.; Zhou, J.; Lu, M.; Zhang, M.; Ding, H.-M.; Chen, Y.; Li, S.-L.; Lan, Y.-Q. Covalent-bonding oxidant on group and titanium cluster to synthesize a porous crystalline catalyst for selective photo-oxidation biomass valorization. *Angew. Chem., Int. Ed.* **2022**, *61* (37), No. e202209289.

(44) Wang, H.; Yang, C.; Chen, F.; Zheng, G.; Han, Q. A crystalline partially fluorinated triazine covalent organic framework for efficient photosynthesis of hydrogen peroxide. *Angew. Chem., Int. Ed.* **2022**, *61* (19), No. e202202328.